PHYSICAL REVIEW B **109**, 214113 (2024)

Mechanism of thermally assisted stabilization of pressure-induced sp^3 bonds in amorphous carbon

Zhidan Zeng,[1,*] Hongwei Sheng,[2] Hongbo Lou,[1] Yongjin Chen,[1] Tao Liang,[1] Xiehang Chen,[3] Fei Zhang,[4]
Konstantin Glazyrin,[5] Hanns-Peter Liermann,[5] and Qiaoshi Zeng[1,6,†]
[1]*Center for High Pressure Science and Technology Advanced Research (HPSTAR), Shanghai 201203, China*
[2]*Department of Physics and Astronomy, George Mason University, Fairfax, Virginia 22030-4444, USA*
[3]*Frontier Center of Energy Distribution and Integration, Tianfu Jiangxi Lab, Chengdu 641419, China*
[4]*Institute of High Energy Physics, Chinese Academy of Sciences, Beijing 100049, China*
[5]*Deutsches Elektronen-Synchrotron DESY, Notkestrasse 85, 22607 Hamburg, Germany*
[6]*Shanghai Key Laboratory of Material Frontiers Research in Extreme Environments (MFree),*
Shanghai Advanced Research in Physical Sciences (SHARPS), Shanghai 201203, China

(Received 1 November 2023; revised 15 April 2024; accepted 13 June 2024; published 27 June 2024)

Various sp^3-bond-rich noncrystalline carbon materials with extraordinary properties have been synthesized through structural transitions of sp^2-bonded amorphous carbon under high pressure and high temperature (HPHT). However, the specific role of pressure and temperature in the process of the structural transition remains elusive due to the lack of *in situ* investigation. Here, combining *in situ* HPHT synchrotron x-ray diffraction and first-principles simulations, we investigated the structural evolution of glassy carbon (GC) (an archetype amorphous carbon) under pressure and thermal annealing. We found GC transformed to a recoverable superstrong amorphous carbon with a considerable number of sp^3 bonds when compressed to ∼58 GPa and annealed at ∼728 K. Our results indicate that thermal annealing (even far below 1000 K) plays a key and unique role in stabilizing the sp^3 carbon bonds by lowering the free energy through local structural rearrangements. Otherwise, most pressure-induced sp^3 carbon bonds could not be preserved upon pressure release. Therefore, temperature is an essential tuning parameter for synthesizing sp^3-bond-rich amorphous carbon with tailorable properties. These results improve our fundamental understanding of the structural transition of amorphous carbon under HPHT and provide crucial guidance for synthesizing novel amorphous carbon materials.

DOI: 10.1103/PhysRevB.109.214113

I. INTRODUCTION

Carbon has numerous allotropes with diverse structures and properties [1]. Among them, amorphous carbon, due to the absence of strict crystalline symmetry, offers large freedom of structure and property tuning by varying its atomic structures and bonding chemistry (e.g., sp, sp^2, and sp^3 hybridization). Utilizing the amorphous to amorphous structural transition under high pressure and high temperature (HPHT), various novel noncrystalline carbon materials with high sp^3 fractions have been synthesized recently, i.e., quenchable amorphous diamond [2], ultrahard amorphous carbon [3,4], and paracrystalline diamond [5]. These noncrystalline carbon materials present extraordinary physical properties such as ultrahigh hardness and strength comparable to diamond, tunable optical band gap, and extraordinary thermal conductivity [3–5]. More amorphous carbon materials with novel properties are expected to be obtained in a wider pressure-temperature phase space. However, the structural transitions of amorphous carbon during the HPHT treatment and the specific roles of pressure and temperature are poorly understood due to the lack of *in situ* studies. Consequently, most of the previous studies rely on an inefficient trial and error strategy with massive synthesis by mapping the pressure-temperature diagram followed by postfabrication property characterization.

Glassy carbon (GC), as a bulk noncrystalline carbon with mostly sp^2 bonds, is an ideal precursor for synthesizing novel amorphous carbon materials through amorphous to amorphous transitions. Recently, the change of structure and properties of GC under high pressure have been extensively studied by *in situ* experiments at room temperature [6–12] or *ex situ* experiments at high temperatures [2,13–17]. At room temperature, GC goes through a pressure-induced reversible (with a large hysteresis), sluggish structural transition into a tetrahedral amorphous carbon (ta-C) with high sp^3 fraction, high mechanical strength and incompressibility, large electrical resistance, and a noticeable band gap [6,7,9,11,12]. The structural transition starts at 22.6–26.0 GPa, and finishes at ∼81 GPa [10]. In addition to experiments, the pressure-induced transitions of GC during "cold compression" have also been intensively studied by simulation [8–10,18]. The evolution of the structure factor of GC with increasing pressure was monitored, indicating a transition from GC to ta-C upon compression. Moreover, the ta-C obtained at high pressure transforms back to GC upon decompression, which is consistent with the experimental results.

In contrast to the reversible transition during cold compression, pressure-induced irreversible transitions in GC were observed when high temperatures are involved, resulting

---

[*] Contact author: zengzd@hpstar.ac.cn

[†] Contact author: zengqs@hpstar.ac.cn

in a series of amorphous and crystalline carbon materials recoverable to ambient conditions with various interesting properties [1,2,13–17,19,20]. Interestingly, the structures of the synthesized carbon materials are highly dependent on the HPHT conditions reached during the experiment. For instance, large-volume press and diamond anvil cell (DAC) HPHT experiments suggest that GC transforms to nanocrystalline diamond at typically 18–21 GPa and 2123–2523 K [13,14], 25 GPa and 1473 K [15], or 25–53 GPa and 1800–2200 K [20]. At relatively lower temperatures, composites of nanocrystalline diamond and disordered multilayer graphene could be synthesized at 25 GPa and 1323–1423 K [17], and compressed GC with superelasticity was obtained at 25 GPa, 1073–1273 K [15]. More interestingly, in experiments at higher pressures, superstrong quenchable amorphous diamond could be synthesized at 40–50 GPa and ∼1800 K [2]. These interesting discoveries indicate that both pressure and temperature play critical roles in dictating the structure and properties of those novel carbon materials, especially amorphous carbon materials, synthesized from GC. However, the mechanism behind those experimental observations is unclear, especially the specific effects of pressure and temperature and their interplay still needs to be addressed.

In this study, by combining *in situ* HPHT x-ray diffraction (XRD) with first-principles calculations, we investigated the structural transition of GC during compression followed by thermal annealing at 728 K and up to 58 GPa. We observed an irreversible transition from GC into a superstrong amorphous carbon, which can be preserved to ambient conditions. Our results clarify the mechanism of pressure and temperature treatment for the transition, which will help guide an effective synthesis of novel amorphous carbon with desirable properties under HPHT.

II. EXPERIMENTS AND SIMULATION

A. *In situ* HPHT synchrotron XRD experiments

GC is nearly fully sp^2 bonded and has a highly disordered structure, consisting of curved carbon sheet fragments, containing pentagons, heptagons, and hexagons [21]. GC is commonly classified into two types based on their synthesis temperatures. The GC samples used in this study (and our previous studies) are type 1 GC purchased from Alfa Aesar. It has a bulk density of $\sim 1.54\ \mathrm{g/cm^3}$ and an ash value below 100 ppm (according to standard DIN 51903). Type 1 GC is typically synthesized at much lower temperatures compared to type 2 GC, resulting in a more disordered atomic structure [22]. The different behavior of type 1 and type 2 GC under high pressure (and temperature) may be attributed to these structural differences [2,6,8,9,12,16].

In situ HPHT XRD experiments were carried out at beamline P02.2 of PETRA III, Deutsches Elektronen-Synchrotron (DESY), Hamburg, Germany. The HPHT experiment was performed using a graphite resistive heated DAC with culet sizes of ∼300 μm [see Fig. 1(a) for the illustration of the assembly]. A graphite disk heater with a hole in the center is placed around the diamond anvils for resistive heating. Two type *R* thermal couples are mounted on the anvil pavilion close to the anvil tip for temperature measurement. The DAC was inserted into a vacuum vessel with two Kapton windows on the x-ray path to avoid oxidation during heating. The pressure was controlled remotely using a membrane system. The room-temperature compression experiment took approximately 1.5 h, and the heating experiment (from room temperature to ∼728 K) took approximately 3 h. More details of the setup can be found in Ref. [23]. A 100 μm diameter hole was drilled in a preindented Re gasket as the sample chamber. GC flakes (type I, from Alfa Aesar) were loaded to fill up the sample chamber without pressure transmitting medium. A tiny piece of Au foil was loaded along with the sample as the pressure standard. The pressure was determined by XRD using the equation of state of Au [24]. Background scattering from the diamond anvils was collected before loading the GC sample into the sample chamber of the DAC and was subtracted to obtain the XRD signal of the sample, which is critical because otherwise the sample signal is invisible due to the poor scattering power of carbon [25]. The x-ray beam was tuned to a wavelength of 0.2895 Å and a size of ∼8 μm × 3 μm. A two-dimensional (2D) PerkinElmer (XRD1621) detector was used for XRD data collection. The software DIOPTAS was used to calibrate the detector parameters using a CeO_2 powder (NIST 647b)

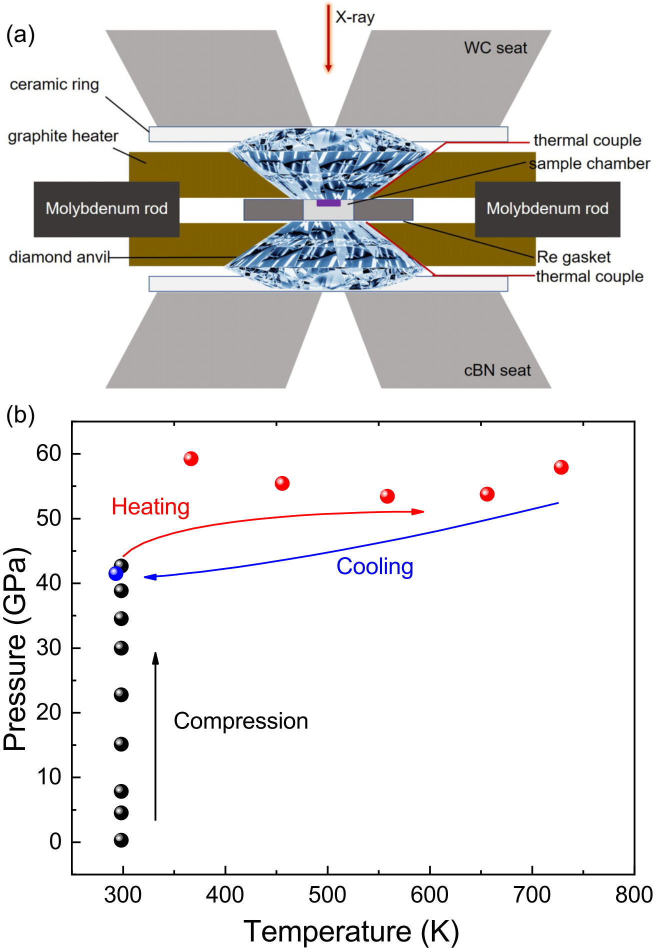

FIG. 1. Schematic of the resistively-heated diamond anvil cell. (a) Schematic of the assembling of the resistively heated diamond anvil cell for *in situ* HPHT XRD experiment. (b) The evolution of pressure and temperature of the experiment.

and to convert the 2D images into one-dimensional (1D) XRD patterns [26].

Synchrotron XRD of the recovered carbon sample was performed at beamline 10 XU, SPring-8. The x-ray wavelength was 0.4147 Å and the beam size was ~3 μm × 2 μm. A Rigaku image plate was used for XRD data collection. CeO_2 powder was used to calibrate the detector parameters. Background scattering from the air was collected and subtracted to obtain XRD patterns of the sample.

B. Micro-Raman spectroscopy experiments

Multiwavelength Raman spectra were collected to characterize the C-C bonds in the initial GC and the recovered sample. Micro-Raman spectroscopy systems (Renishaw, in-Via Reflex) with various excitation lasers were used, i.e., 532, 633, 830, and 325 nm. For the 325 nm laser, a 40× ultraviolet (UV) objective lens was used in the experiments. For the other experiments, a 20× objective lens was employed. The total collection time for each Raman spectrum varied from 60 to 300 s. The *D* band and *G* bands in the Raman spectra were fitted to a Lorentz function and a Breit-Wigner-Fano (BWF) function, respectively [27].

C. Transmission electron microscope (TEM) experiments

The TEM samples were prepared using a FEI Versa three-dimensional (3D) dual-beam focused ion beam (FIB). The voltage and current of the FIB were reduced from 5 kV and 30 nA to 5 kV and 16 pA, respectively, followed by a 2 kV and 4.3 pA beam during sample thinning to minimize the possible damage from the Ga-ion beam to the sample. The TEM experiments were performed using a JEOL JEM-F200 TEM with an accelerating voltage of 80 kV. High-resolution TEM images, selected area electron diffraction (SAED) pattern, carbon *K*-edge electron energy loss spectroscopy (EELS), and low-loss EELS were collected both on the initial GC and the HPHT recovered carbon sample. The energy resolution of the EELS was 0.5 eV.

D. First-principles calculations

First-principles calculations based on the Vienna *Ab Initio* Simulation Package (VASP) [28] were performed to obtain the evolution of the atomic structure of GC under HPHT. The projector augmented wave potential (PAW) with a valence configuration of $2s2p$ and the generalized gradient approximation (GGA) were used in the simulation [29]. We applied the optPBE-vdW functional to treat the van der Waals interactions [30]. The kinetic energy cutoff was set to 400 eV, and the simulation was conducted on the gamma point only. The simulation method is similar to that used in previous studies to investigate the phase transition mechanism of GC under high pressure at room temperature [9,10]. Liquid carbon (1024 atoms) was quenched with a fixed density of 2.1 g/cm^3 from 5000 K at a cooling rate of 5×10^{13} K/s using *ab initio* molecular dynamics (MD) simulation to obtain the initial GC sample in an *NVT* ensemble. The process involves approximately 10 ps for the initial GC model preparation (liquid quenching), during which we observe a complete phase transition from liquid carbon to glassy carbon around 4000 K. This phase transition is depicted in Fig. S1 of the Supplemental Material [31] (also see [32,33]), where the potential energy is plotted against temperature during the quenching process.

To simulate the compression and decompression processes of GC, the simulation box size was scaled with small steps, followed by conjugate gradient geometric optimization to achieve the minimum energy state of the structure at 0 K. The sample was gradually compressed to ~100 GPa, followed by annealing at 1500 or 1000 K for 6 ps. The annealing time was set to be long enough to allow the system to achieve the minimum energy state. The pressure dropped to 85.5 GPa after 1500 K annealing, and to 87.7 GPa after 1000 K annealing. The initial sample (~100 GPa, before annealing), 1500 K annealed sample, and 1000 K annealed sample were further equilibrated at 300 K for 2 ps, and the cohesive energy and pressures were calculated. The radial distribution function $g(r)$ and the structure factor $S(q)$ were calculated based on a large structure model of GC with 1024 atoms.

Calculating Raman spectra of GC is challenging due to the large system (1024 atoms) and the high computational cost for the density functional perturbation theory (DFPT), which renders the calculation of the polarizability tensors (at each MD step) intractable. Alternatively, the vibrational density of states from the dynamical matrix, which correlates with the Raman active modes, was calculated. The calculated vibration density of states (VDOS) for glassy carbon and ta-C (~80% sp^3 bonding) are shown in Fig. S2 of the Supplemental Material [31] (also see [32,33]).

It should be noted that recently significant advancements have been made in machine learning potential [34–36], which we plan to explore in our future work. In this study, we opted for the time-consuming *ab initio* MD approach for two primary reasons. First, we were concerned about the local bonding change under high pressure, and the structure features on the mesoscale (e.g., porosity) were not our primary focus. Second, despite the advances of the machine learning potential in the literature, our experimental investigation covers a wide pressure range (0–60 GPa), within which we believe our *ab initio* simulation method would yield more reliable results than the empirical simulation methods.

III. RESULTS AND DISCUSSION

A. Structure evolution of GC during compression and annealing

In the *in situ* HPHT synchrotron XRD experiment, the GC sample was first compressed to ~42.7 GPa at room temperature, followed by heating to ~728 K [see Fig. 1(b)]. During the heating process, despite the fact that a membrane system was used to stabilize the pressure, the pressure still increased to ~58.0 GPa at 728 K most likely due to the extra force applied to the anvils from thermal expansion of the DAC parts [23]. After heating, the pressure dropped back to ~41.5 GPa once the DAC cooled down to room temperature.

Figure 2(a) shows representative XRD patterns of the GC sample during compression and heating. The XRD pattern of GC shows two broad characteristic peaks, the first diffraction peak (FDP) and the second diffraction peak (SDP), associated with the average interlayer and intralayer characteristic distances in GC, respectively [21]. Consistent with previous

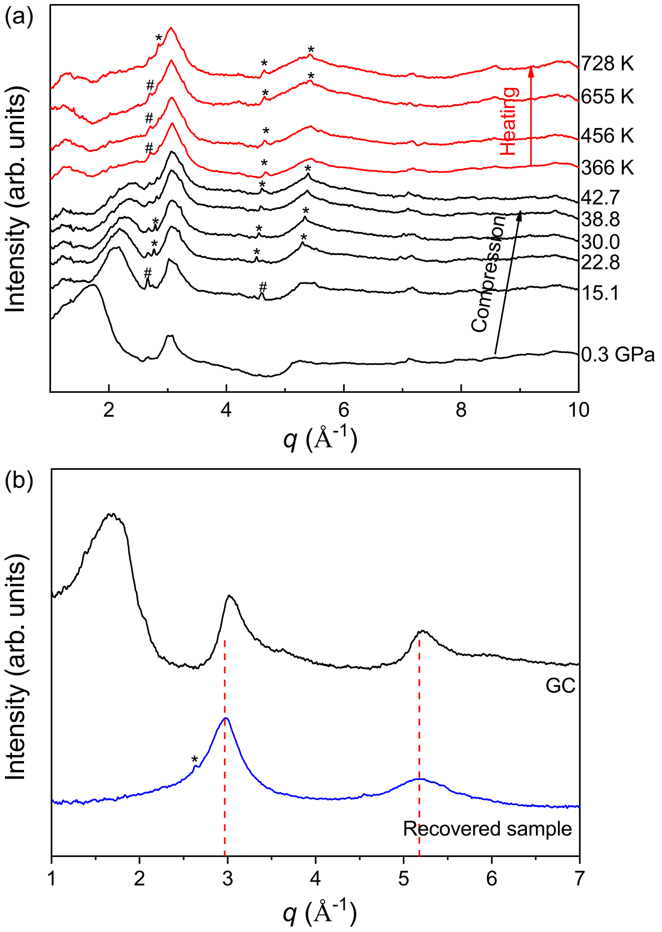

FIG. 2. *In situ* HPHT XRD patterns. (a) Representative XRD patterns of GC during compression up to 42.7 GPa (black lines) and heating up to 728 K (red lines). The x-ray wavelength is 0.3220 Å. The numbers on each pattern are the pressures/temperatures where the patterns were collected. (b) XRD pattern of the amorphous carbon sample recovered from 58 GPa and 728 K compared with that of the as-received GC. The data were collected outside the DAC. Diffraction peaks from the pressure calibrant Au and gasket Re are marked by * and #, respectively.

high-pressure XRD results at room temperature, the intensity of the FDP decreases with increasing pressure above 22.8 GPa, implying that a structural transition takes place in GC [9]. More notably, during annealing, the intensity of the FDP was observed to drop further, and the FDP becomes almost invisible at ~728 K (and 58 GPa). In contrast, previous studies showed that the FDP of GC remains noticeable when it is compressed to a similar pressure (51.4 GPa) at room temperature [9,10]. These observations demonstrate that heating could effectively promote the phase transition in GC.

Since the main peak of the high-pressure carbon phase largely overlaps with the SDP of GC, to obtain more detailed information on this phase transition, we fit the peak at $\sim 3.10\,\text{Å}^{-1}$ to the Gaussian function. Figures 3(a) and 3(b) show the peak positions as a function of pressure and annealing temperature, respectively. The peak positions were converted to $2\pi/q$, which corresponds to average characteristic intralayer atomic distances in the real space. As shown in Fig. 3(a), the peak at $\sim 3.10\,\text{Å}^{-1}$ (~2.03 Å) shifts to smaller d spacing with increasing pressure at the beginning of compression, then keeps a nearly constant or slightly increasing trend at ~22 GPa. This abnormal crossover can be attributed to the beginning of a sluggish transition to a sp^3-bonded high-pressure ta-C according to the previous room-temperature studies [9,10]. Since the main peak of the high-pressure ta-C overlaps with the SDP of GC, the GC to ta-C phase transition results in an abnormal pressure dependence of the SDP peak position of GC, as shown in Fig. 3(a).

Upon heating, the peak shifts to larger d spacing with increasing temperature, which at first glance seems to reflect the thermal expansion effect of the sample. In fact, several factors need to be taken into account herein, including thermal expansion, drift of pressure, and phase transition. Due to the ultrastrong C-C covalent bonding, carbon materials usually have extremely low thermal expansion coefficients. Assuming a thermal expansion coefficient similar to that of graphite (in the "a" direction, $\sim -1.2 \times 10^{-6}$ to $5 \times 10^{-7}\,\text{K}^{-1}$ from room temperature to 900 K) [37], we estimate that a temperature increase of ~430 K in the experiment (from room temperature to 728 K) would result in a peak shift of less than ~0.02%. This change is two orders of magnitude lower than the peak shift observed in our experiment (~1.4%). Therefore, the effect of thermal expansion can be neglected herein. On the other hand, the pressure of the sample might change during heating due to the thermal expansion of the DAC parts. As shown in Figs. 1(b) and 3(b), in our experiment, the pressure increased from 42.7 to 59.2 GPa when the sample was heated to 366 K, and then it remained relatively stable during further heating to 728 K. However, the higher pressure would lead to a peak shift to smaller d spacing; hence it cannot explain the "lattice expansion" observed in our experiment. Therefore, the unusual "lattice expansion" with increasing temperature can be attributed mainly to a thermally promoted structural phase transition. The continuous peak shift implies that the phase transition is sluggish and continuous. Moreover, comparing the XRD data collected at room temperature before annealing (at 42.7 GPa) and after annealing (at 41.5 GPa), the apparent difference in peak position at similar pressures [see Fig. 3(b)] further confirms the irreversible phase transition during the annealing process.

B. Structure and properties of the recovered sample

To obtain high-quality XRD data of the sample, after decompression, we removed the sample from the DAC and collected its XRD data at ambient conditions. As shown in Fig. 2(b), the XRD pattern of the recovered sample does show distinct features from that of the initial GC; i.e., the FDP of GC is not visible anymore in that of the recovered carbon sample, and the peaks at ~3.0 and $\sim 5.3\,\text{Å}^{-1}$ show different peak positions and shapes. The distinct XRD patterns suggest that the high-pressure high-temperature treatment used in this study has induced an irreversible structural phase transition of GC, resulting in a quenchable amorphous carbon (AC) with a different structure.

We further investigate the properties of the AC sample. Figures 4(a) and 4(b) show optical microscope images of the sample collected with reflected and transmitted light,

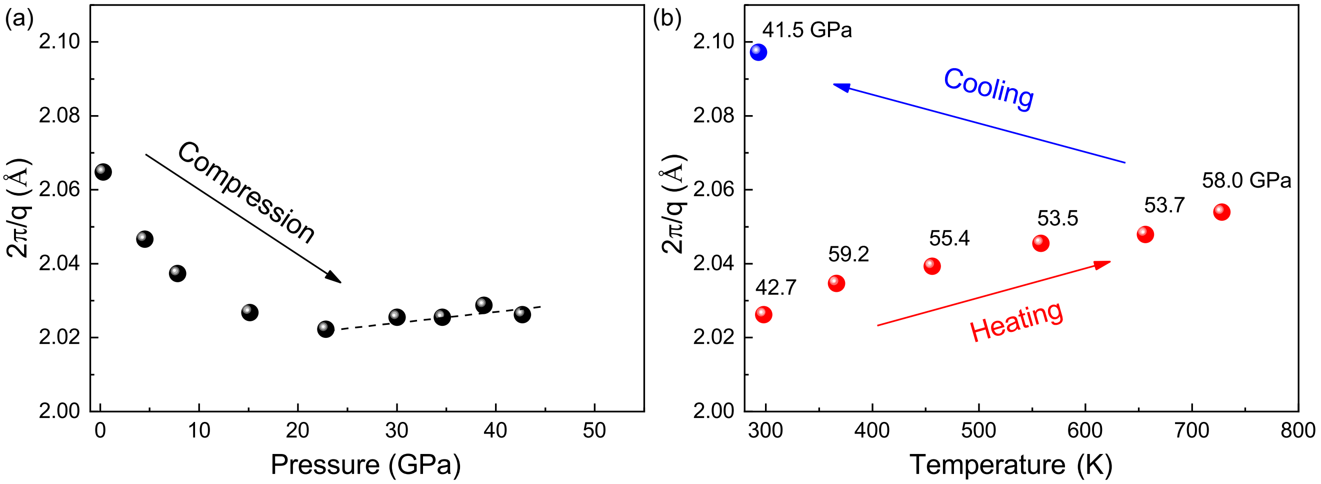

FIG. 3. Structural evolution during compression and heating. (a) The position of the peak at approximately 3.0 Å^{-1} as a function of pressure during compression up to 42.7 GPa (black circles). (b) The position of the peak at approximately 3.0 Å^{-1} as a function of temperature during heating up to 728 K (red circles) and cooling down to 293 K (blue circle). The peak positions were converted to $2\pi/q$, which corresponds to average characteristic intralayer atomic distances in the real space. The peak positions were derived by fitting the diffraction peaks to Gaussian functions. The dashed line serves as a guide to the eye.

respectively. In contrast to the opaque GC, AC is translucent and presents a dark-red color with transmission light. After removing the sample from the DAC, ring cracks are present on both diamond anvils [see Figs. 4(c) and 4(d)]. The occurrence of ring cracks on the anvil is usually associated with an ultrahigh pressure gradient in the diamond anvils during the experiments. One typical case is that a superhard material indents diamond anvils under high pressure [38]. Ring cracks were also observed in previous studies on the high-pressure phases of graphite and fullerenes, in which the high-pressure carbon phases were believed to be superhard [38–40]. Therefore, the occurrence of ring cracks in our study indicates that AC could be a superstrong material with low compressibility.

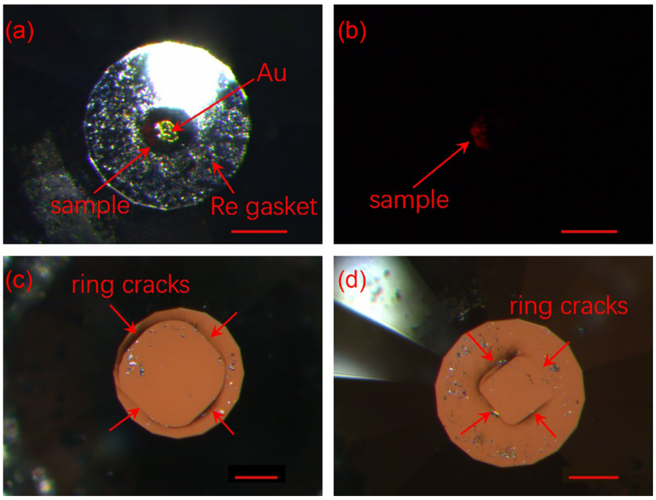

FIG. 4. Optical microscope images of the sample and anvils. (a) Optical microscope image of the amorphous carbon sample recovered from 58 GPa and 728 K illuminated by both reflective and transmitted light (a) and by transmitted light alone (b) Optical microscope image of the anvils on the piston side (c) and cylinder side (d) of the DAC after pressure release. The scale bars represent 100 μm.

To deepen our understanding of the structure and chemical bonding of the AC, we compared the Raman spectra of the AC and GC samples in Fig. 5(a). The *D* and *G* bands of AC are significantly broader than those of GC. The broadening of the *D* and *G* bands is usually associated with the disordering of the atomic structure [27]. Meanwhile, compared with GC, the relative intensity of the two peaks in AC also changes due to the obviously weaker *D* band of AC. By fitting the *D* and *G* bands to Lorentz and BWF functions [41], we obtained the peak height ratio *I*(*D*)/*I*(*G*). The *I*(*D*)/*I*(*G*) is 0.83 for GC, and 0.75 for AC. Since the *D* band in amorphous carbon is usually attributed to the breathing modes of the sixfold rings of carbon atoms and its intensity is proportional to the number of the rings [27], the weaker *D* band [smaller *I*(*D*)/*I*(*G*)] in AC implies that a fraction of the sixfold rings in GC has been destroyed most likely due to the sp^2 to sp^3 transition. Therefore, the Raman results suggest that the original layered atomic structure of GC has been altered during the transition to AC under HPHT, which is consistent with the observation of changes in XRD results.

We also investigated the dispersion of the *G* band using multiwavelength Raman spectra [see Figs. 5(b)–5(d)]. As shown in Figs. 5(c) and 5(d), the *G* band of AC shifts to a higher frequency with increased excitation energy, while the *G* band of GC does not show a noticeable shift. The quantitative results were obtained by fitting the *D* and *G* bands to Lorentz and BWF functions, respectively [41]. As shown in Fig. 5(b), the *G* band position of GC remains unchanged in all the experiments, consistent with previous results [42]. In contrast, evident dispersion of the *G* band is observed in AC, i.e., the *G* band shifts to a lower wave number with increasing laser wavelengths with a slope of –0.138(8) $\text{cm}^{-1}\,\text{nm}^{-1}$. *G* band dispersion is only observed in amorphous carbon, and the degree of dispersion is proportional to the degree of

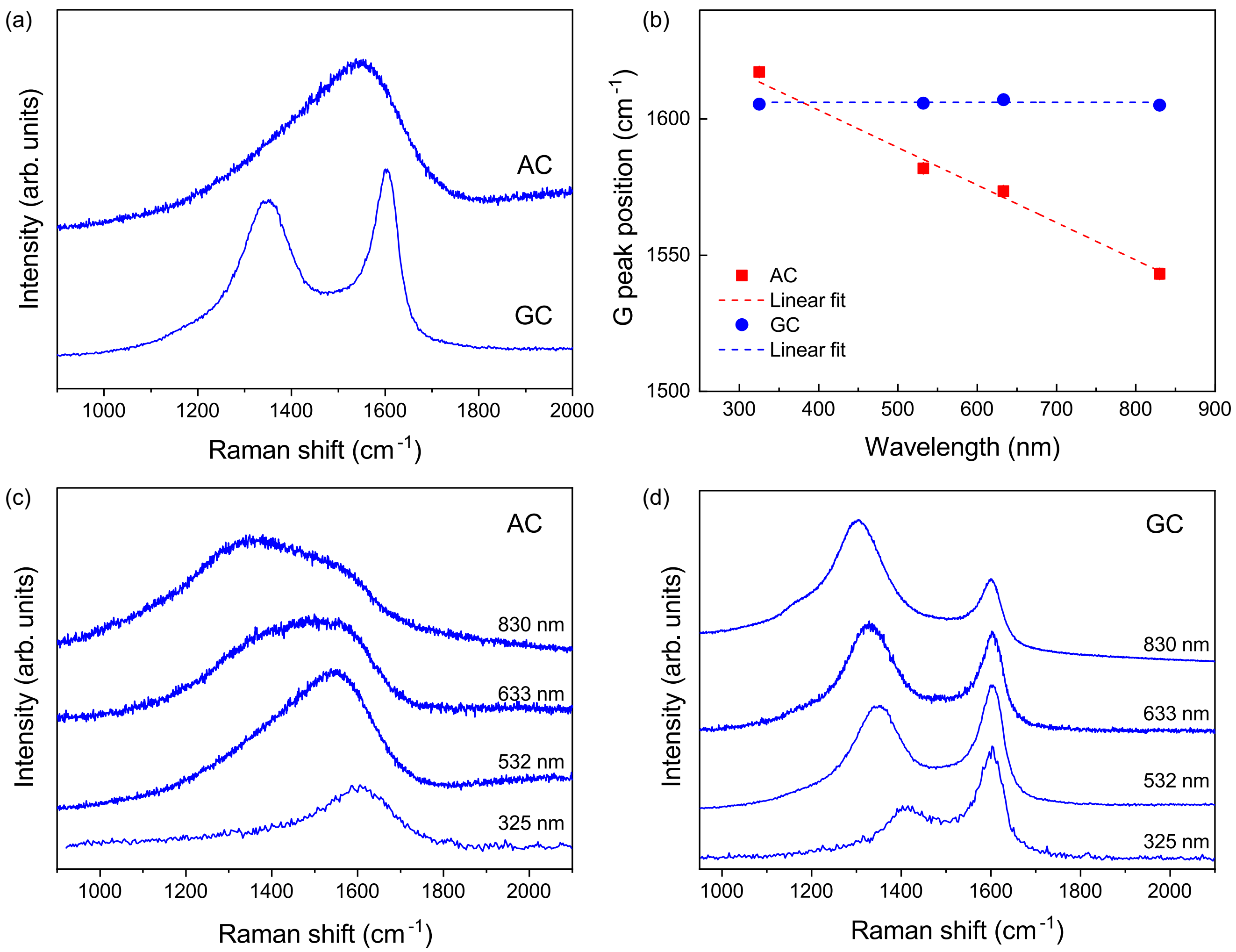

FIG. 5. Multiwavelength Raman spectroscopy. (a) Raman spectra of GC and AC with 532 nm excitation laser. (b) The *G* peak position as a function of the wavelength of excitation lasers. The *D* peak and *G* peaks were fit to a Lorentz and BWF function, respectively. The errors of fitting are smaller than the symbol size. Multiwavelength Raman spectra of AC (c) and GC (d). The spectra have been shifted vertically for better visibility. For the Raman spectrum of AC collected using a 830 nm laser, a linear background was subtracted to remove the strong fluorescence signal.

disorder of the sp^2-bonded carbon atoms, which usually increases with increasing sp^3 bond fraction [43]. Therefore, the *G* band dispersion observed in the AC suggests the sample consists of a highly disordered atomic structure and is a sp^3-bond-rich carbon material.

Furthermore, we compared the high-resolution transmission electron microscopy (HRTEM) images and SAED patterns of AC with those of GC. As shown in Figs. 6(a) and 6(b), GC presents a curved layered structure with an interlayer distance larger than 3 Å, which corresponds to the innermost diffraction ring in the SAED pattern. The atomic packing in the AC sample seems denser and more random due to the disappearance of the layered features [see Fig. 6(c)]. The changes in the HRTEM image are also consistent with those in SAED, in which the innermost diffraction ring of GC [see Fig. 6(b)] is not visible in the SAED of AC [see Fig. 6(d)]. The changes in SAED agree well with the XRD results. The nature of the carbon bonds in AC was investigated by carbon *K*-edge EELS [see Fig. 6(e)]. For AC, the peak at ~284 eV, which corresponds to C-C π bonding, has a much lower intensity than that of GC. Using GC as a fully sp^2-bonded standard material, the sp^3 fraction of AC is estimated to be approximately 50% based on the peak area ratio between the π^* and σ^* signals (using a two-window method with window widths of 4 and 10 eV, respectively) [44]. The plasmon peak observed in the low-loss EELS is centered at ~27.0 eV, in contrast to the much lower value of 23.5 eV for GC [see Fig. 6(f)]. By assuming the plasmon peak of diamond located at 34.0 eV [45], the density of AC is estimated to be ~2.80 g/cm^3. This density is consistent with the sp^3 fraction of approximately 50% [27]. It should be noted that the absolute value of the center of the plasmon peak would be affected by the uncertainty in the calibration of the spectrometer in EELS measurement and the parameters used in peak fit; hence it may vary slightly in different studies.

C. First-principles calculations

All the above-mentioned experimental results indicate that GC went through a continuous and sluggish structural

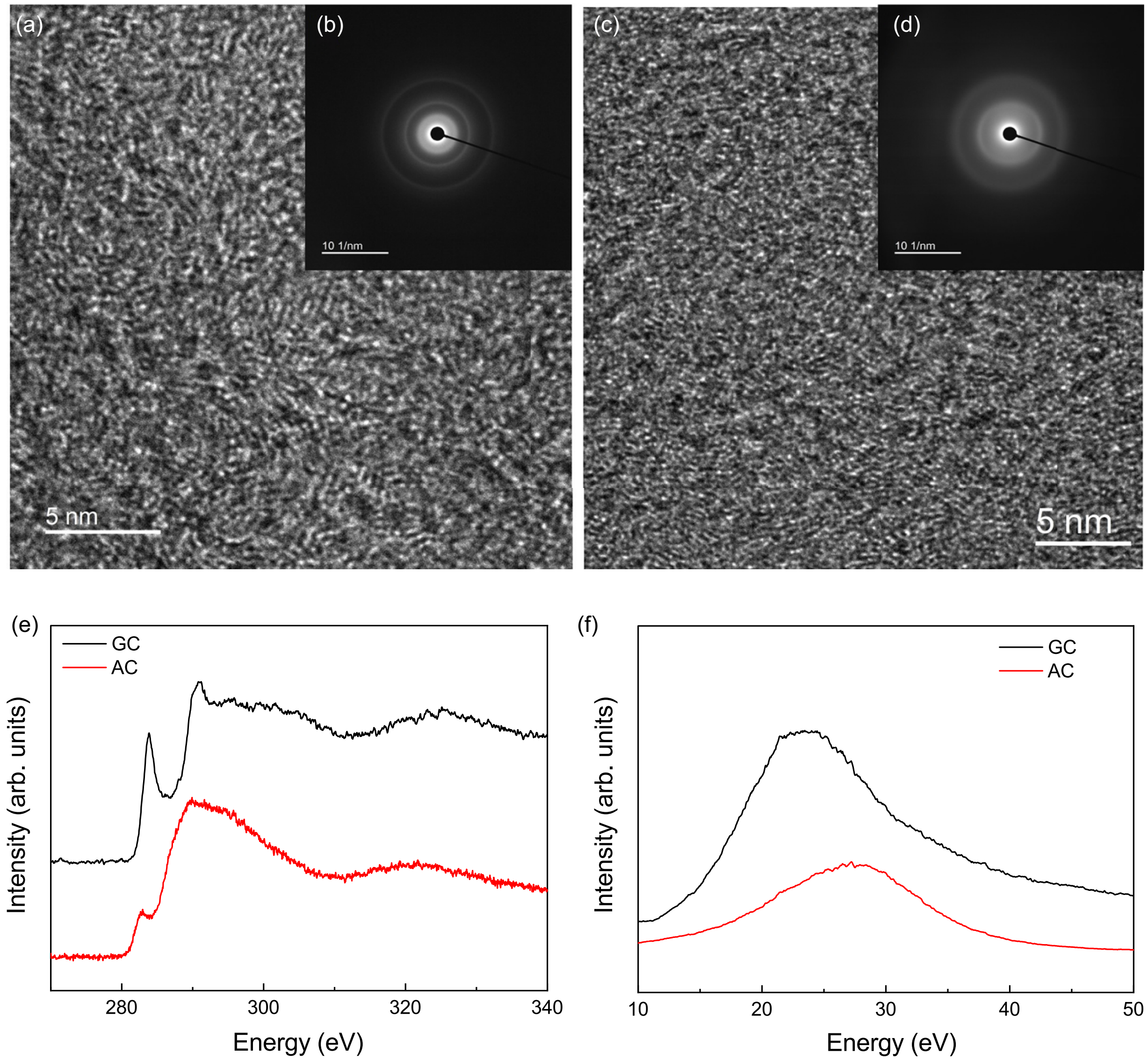

FIG. 6. TEM studies of the recovered sample. HRTEM image (a) and selected area electron diffraction (SAED) image (b) of GC; HRTEM (c) and SAED images (d) of the recovered sample AC. The scale bars in (a), (c) represent 5 nm. (e) Carbon *K*-edge EELS of GC (black) and the recovered sample AC (red). (f) The plasmon peak of GC (black) and the recovered sample AC (red).

transition during compression and annealing. In contrast to the reversible transition observed in room-temperature compression up to 93 GPa or to even higher pressures [10,11], the transition under high pressure (58 GPa) and moderate temperature (728 K) becomes irreversible, pointing to the essential role of thermal treatment in the transition. To understand the effect of thermal treatment at the atomic level, we employed *ab initio* molecular dynamics (MD) simulation to investigate the transition.

In the simulation, the GC sample was firstly compressed to ~100 GPa at 0 K, followed by annealing at 1500 K for 6 ps. The starting GC has a fully sp^2-bonded layered structure, which is consistent with experimental observation (more details can be found in Refs. [9,10]). As shown in Fig. 7(a), upon compression to ~100 GPa, the structure of the sample has transformed from a fully sp^2-bonded layered structure to a sp^3-bond-dominated tetrahedral network structure with a sp^3-bond fraction of ~85.5%. After thermal annealing, the overall change in the atomic configuration seems not significant; we still notice fewer sp^2-bonded atoms (in gray) in the annealed structure [see Figs. 7(a) and 7(b)]. The sp^3 fraction increases from ~85.5% to ~92.4% according to the average coordination number of C atoms in the structure model. The increased sp^3 fraction suggests that thermal annealing promotes the sp^2 to sp^3 transition, which is consistent with our experimental observation. Figures 7(c) and 7(d) compare the structure factor $S(q)$ and radial distribution function $g(r)$ of the sample before and after annealing. After annealing, the two strongest peaks at ~3.2 and 5.7 Å^{-1} in $S(q)$ remain almost the same, but the peaks in the higher-q region change slightly. The changes in the real space [$g(r)$] are more visible. The first peak of $g(r)$ (at ~1.5 Å), which roughly corresponds to the first nearest-neighbor shell, shifts to larger r, and becomes more sharpened [see Fig. 7(d) inset]. By fitting the first peak to a Gaussian function, we found the full width at half maximum (FWHM) of the peak decreased by ~5% after

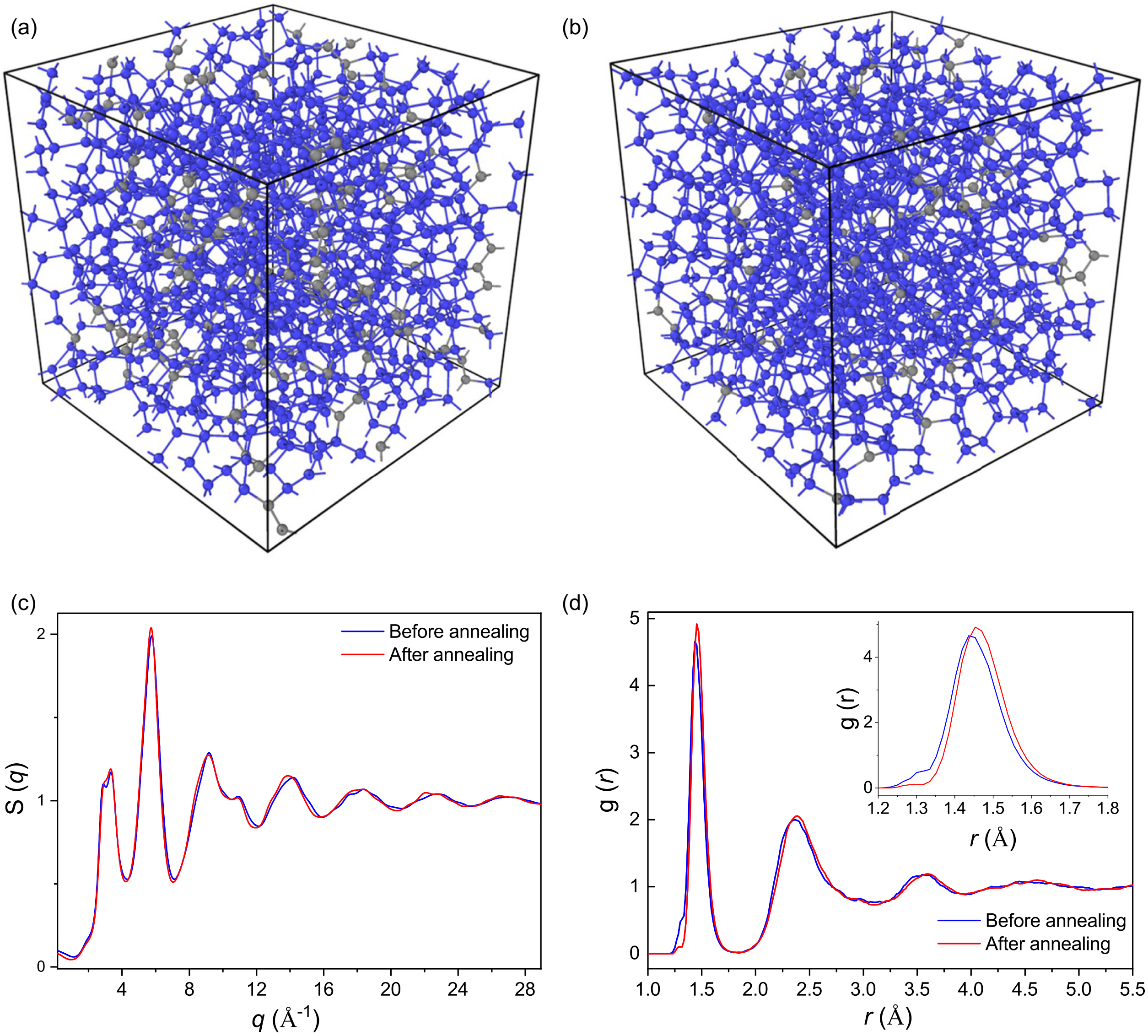

FIG. 7. Simulation of atomic structure of GC during HPHT treatment. Atomic configuration of GC compressed to ∼100 GPa (a), and annealed at 1500 K (b). The blue and gray spheres represent sp^3-bonded C atoms and sp^2-bonded C atoms, respectively. (c) Structure factor $S(q)$ of the amorphous carbon before (blue curve) and after 1500 K annealing (red curve). (d) Radial distribution functions $g(r)$ of the amorphous carbon before (blue curve) and after 1500 K annealing (red curve). The inset shows a zoom-in of the first $g(r)$ peak.

annealing. The increased average atomic bond length after annealing is in line with the higher sp^3 fraction in the annealed sample, because the sp^3 C-C bonds are usually longer than sp^2 bonds. For instance, at ambient pressure, C-C bond length is 1.54 Å for sp^3 bonds in diamond, in contrast to the 1.42 Å for sp^2 bonds in graphite. Meanwhile, the enhanced intensity and lowered FWHM of the first g(r) peak further suggest the bond length in the annealed sample is more uniform with a narrower distribution (less distortion). In contrast, without thermal annealing, the sp^3-dominated structure obtained by room-temperature compression is typically highly distorted and strained [10], and the local strain energy could be very high due to the superstrong C-C covalent bonds. The uniformity in bond length would help to reduce the strain and lower the free energy of the system. Consistent with our expectation, the cohesive energy of the sample decreases by ∼0.1 eV/atom (from −8.051 to −8.154 eV/atom) after thermal annealing, which contributes to the enhanced stability of the sp^3-bonded carbon.

We further investigate the stability of the annealed sample during decompression. Figure 8 shows the sp^3 fraction of the annealed sample as a function of pressure, in which the data of a cold-compressed (at 0 K) GC sample were also included for comparison [9]. In contrast to the obvious reversible sp^2 to sp^3 transition in the sample without thermal annealing, most sp^3 bonds in the annealed sample remain stable upon decompression. On the other hand, in our previous simulation without annealing, despite being compressed to an extremely high pressure (198 GPa), the high-pressure phase with sp^3 fraction up to 90% is still not quenchable after pressure release [10]. These distinct results suggest the stability of the high-pressure amorphous carbon cannot be improved simply

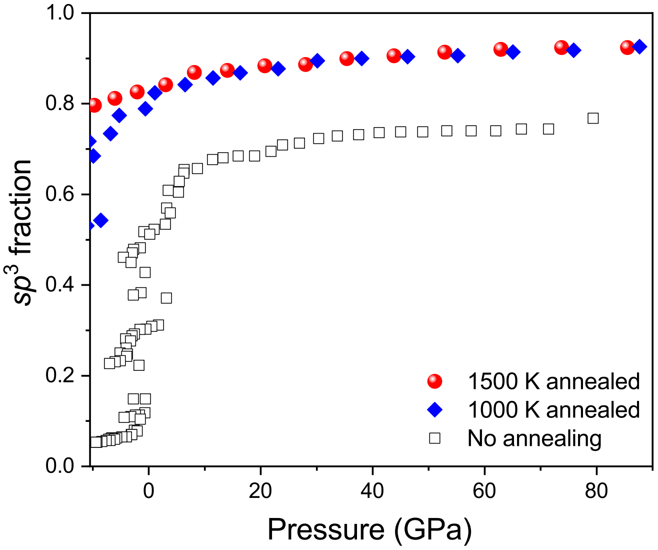

FIG. 8. Stability of the high-pressure sp^3-bonded amorphous carbon. The fraction of sp^3 bonds in amorphous carbon as a function of pressure during decompression. GC was first compressed to approximately 100 GPa, followed by annealing at 1500 K (red circles), or at 1000 K (blue diamonds) before decompression. Open squares represent data from the cold compression experiment, in which GC was compressed to ~80 GPa, then decompressed directly without annealing (from Ref. [9]).

by achieving a higher sp^3 fraction by "cold compression." Although the sp^3 bonds will partially transform back to sp^2 bonds for the annealed sample, most of the sp^3 bonds can be preserved after pressure release. A higher annealing temperature could preserve more sp^3 bonds; e.g., as shown in Fig. 8, the sp^3 fraction of the annealed sample decreases slightly from ~92.4% to ~79.7% for the 1500 K annealed sample and from 91.8% to 68.5% for the 1000 K annealed sample after pressure release. These results suggest that the atomic structure adjustment associated with strain release during thermal annealing is essential to stabilizing the sp^3-bonded structure obtained by compression, which thus renders it preservable at ambient conditions. Moreover, although GC was studied in our simulation as a model system, the simulation results could also provide insight into the synthesis of sp^3-bonded amorphous carbon from other carbon precursors, such as the recently reported transition from fullerenes to ultrahard amorphous carbon under HPHT [3–5]. Similar to the case of GC, those previous *ex situ* experiments on fullerenes and simulations show that the ultrahard amorphous carbon with an extremely high sp^3 content could only be recovered when thermal annealing is involved rather than cold compression [3–5,34,46]. Furthermore, at the same pressure, the sp^3 fraction increases with elevated annealing temperature, which is also consistent with our simulation results.

In addition, it should be noted that due to the lack of strict crystalline symmetry, the topological structure of amorphous carbon has extra freedom of structural flexibility and can be quite different even with the same fraction of sp^3 bonds. Hence, although the sp^3 fraction is an important indicator for the structure of amorphous carbon, the structural stability, as well as other properties of amorphous carbon, is highly dependent on the details of its topological structure. For instance, two amorphous carbon samples with similar sp^3 fraction (92.4% versus 91.8%) in our simulation show distinct stabilities at ambient conditions (Fig. 8) resulting from different thermal annealing temperatures. Therefore, our simulation results demonstrate that thermal annealing temperature is a powerful and sensitive tuning parameter for synthesizing different high sp^3 content amorphous carbon materials through the sp^2 to sp^3 transition under high pressure. These results also highlight the essential role of thermal annealing in stabilizing the sp^3 bonds in amorphous carbon.

Regarding the pressure effect, based on the comparison of our results with previous studies [15], it is suggested that there is a critical pressure (between 25 and 58 GPa for GC) below which the amorphous carbon with high sp^3 fraction cannot be obtained under HPHT conditions. Moreover, under a constant pressure above a critical value, the structure and sp^3 fraction of the recovered amorphous carbon can be effectively tuned by controlling the annealing temperatures.

The pressure-induced structural transition in glassy carbon has been extensively investigated recently, yielding a variety of results. These diverse phenomena may be attributed to the different types of glassy carbon used in various studies and the different levels of shear stress involved [22]. In previous studies on type 1 glassy carbon (from Alfa Aesar, with a highly disordered structure), glassy carbon undergoes a mostly reversible structural transition into a sp^3-bonded tetrahedral amorphous carbon upon compression at room temperature [6,7,9–11]. With the aid of high-temperature annealing, as shown in the current study (58 GPa and 728 K), irreversible transition from glassy carbon to amorphous carbon with a considerable number of sp^3 bonds was observed. The previous studies on type 2 glassy carbon (Sigradur-G from Hochtemperatur-Werkstoffe, with a relatively more ordered graphitic nanostructure) have observed graphitization of glassy carbon after compression to over 45 GPa at room temperature [8], and nanocrystalline diamond and lonsdaleite in the sample recovered from above 80 GPa [47]. Nanocrystalline hexagonal diamond was observed in the samples recovered from 100 GPa and 400 °C [16,19]. The ordered graphitic structure in type 2 glassy carbon may promote the formation of crystalline phase under high pressure. On the other hand, shear stress also plays an important role in the phase transition of carbon materials. Shear-induced diamond formation has been observed in a graphite sample upon decompression at room temperature [48]. Previous studies on glassy carbon have also found that shear stress enhances sp^2 to sp^3 transition in glassy carbon under high pressure and promotes glassy carbon to diamond transition [9,11,16,49]. In our previous simulation, a comparison between uniaxial compression and hydrostatic compression of glassy carbon also indicated an enhanced sp^2 to sp^3 transition under uniaxial compression [9]. Shear stress may also contribute to the formation of superstrong amorphous carbon in this study.

IV. CONCLUSION

In this study, combining *in situ* HPHT XRD and first-principles simulations, we investigated the pressure and temperature effects on the structural evolution of an archetype amorphous carbon (GC) during compression and thermal annealing. We found GC transformed to a superstrong amorphous carbon with a considerable number of sp^3 bonds after compression to ∼58 GPa and annealing at moderate temperature (728 K), which can be preserved to ambient conditions. Our study reveals that elevated temperature (thermal annealing) does play a unique role in stabilizing the pressure-induced sp^3 bonds in the initially sp^2-bonded carbon materials, through local structural adjustments to lower the cohesive energy of the compressed samples. By clarifying the pressure and temperature effects on the formation of sp^3-bonded amorphous carbon materials, this work demonstrates that, above a critical pressure, temperature can be another independent dimension for synthesizing amorphous carbon materials with tailored structure and properties. For example, by using GC as a precursor and controlling the annealing temperatures at different pressures, it is likely that one can obtain a wide range of amorphous carbon materials with a tunable sp^3 fraction (e.g., from ∼50% to nearly 100%), correspondingly with various mechanical, optical, and thermal properties.

ACKNOWLEDGMENTS

The authors thank Dr. Saori Kawaguchi, Dr. Hirokazu Kadobayashi, and Dr. Anna Pakhomova for their help in the synchrotron XRD experiments. The authors acknowledge the financial support from Shanghai Science and Technology Committee, China (Grant No. 22JC1410300) and Shanghai Key Laboratory of Material Frontiers Research in Extreme Environments, China (Grant No. 22dz2260800). We acknowledge DESY (Hamburg, Germany), a member of the Helmholtz Association HGF, for the provision of experimental facilities. Parts of this research were carried out at beamline P02.2, PETRA-III, and the beam time was allocated for proposal I-20180185. Part of the XRD work was performed at the beamline BL 10XU, SPring-8 under Proposal No. 2018B1055, and beamline 15U1, SSRF, China.

[1] B. Sundqvist, Carbon under pressure, Phys. Rep. **909**, 1 (2021).

[2] Z. Zeng, L. Yang, Q. Zeng, H. Lou, H. Sheng, J. Wen, D. J. Miller, Y. Meng, W. Yang, W. L. Mao *et al.*, Synthesis of quenchable amorphous diamond, Nat. Commun. **8**, 322 (2017).

[3] Y. Shang, Z. Liu, J. Dong, M. Yao, Z. Yang, Q. Li, C. Zhai, F. Shen, X. Hou, L. Wang *et al.*, Ultrahard bulk amorphous carbon from collapsed fullerene, Nature (London) **599**, 599 (2021).

[4] S. Zhang, Z. Li, K. Luo, J. He, Y. Gao, A. V. Soldatov, V. Benavides, K. Shi, A. Nie, B. Zhang *et al.*, Discovery of carbon-based strongest and hardest amorphous material, Natl. Sci. Rev. **9**, nwab140 (2021).

[5] H. Tang, X. Yuan, Y. Cheng, H. Fei, F. Liu, T. Liang, Z. Zeng, T. Ishii, M.-S. Wang, T. Katsura *et al.*, Synthesis of paracrystalline diamond, Nature (London) **599**, 605 (2021).

[6] Y. Lin, L. Zhang, H.-k. Mao, P. Chow, Y. Xiao, M. Baldini, J. Shu, and W. L. Mao, Amorphous diamond: A high-pressure superhard carbon allotrope, Phys. Rev. Lett. **107**, 175504 (2011).

[7] M. Yao, J. Xiao, X. Fan, R. Liu, and B. Liu, Transparent, superhard amorphous carbon phase from compressing glassy carbon, Appl. Phys. Lett. **104**, 021916 (2014).

[8] T. B. Shiell, D. G. McCulloch, D. R. McKenzie, M. R. Field, B. Haberl, R. Boehler, B. A. Cook, C. de Tomas, I. Suarez-Martinez, N. A. Marks *et al.*, Graphitization of glassy carbon after compression at room temperature, Phys. Rev. Lett. **120**, 215701 (2018).

[9] Z. Zeng, H. Sheng, L. Yang, H. Lou, L. Tan, V. B. Prakapenka, E. Greenberg, and Q. Zeng, Structural transition in cold-compressed glassy carbon, Phys. Rev. Mater. **3**, 033608 (2019).

[10] L. Tan, H. Sheng, H. Lou, B. Cheng, Y. Xuan, V. B. Prakapenka, E. Greenberg, Q. Zeng, F. Peng, and Z. Zeng, High-pressure tetrahedral amorphous carbon synthesized by compressing glassy carbon at room temperature, J. Phys. Chem. C **124**, 5489 (2020).

[11] M. Yao, X. Fan, W. Zhang, Y. Bao, R. Liu, B. Sundqvist, and B. Liu, Uniaxial-stress-driven transformation in cold compressed glassy carbon, Appl. Phys. Lett. **111**, 101901 (2017).

[12] T. B. Shiell, C. de Tomas, D. G. McCulloch, D. McKenzie, A. Basu, I. Suarez-Martinez, N. Marks, R. Boehler, B. Haberl, and J. Bradby, *In situ* analysis of the structural transformation of glassy carbon under compression at room temperature, Phys. Rev. B **99**, 024114 (2019).

[13] H. Sumiya and T. Irifune, Hardness and deformation microstructures of nano-polycrystalline diamonds synthesized from various carbons under high pressure and high temperature, J. Mater. Res. **22**, 2345 (2007).

[14] N. A. Solopova, N. Dubrovinskaia, and L. Dubrovinsky, Synthesis of nanocrystalline diamond from glassy carbon balls, J. Cryst. Growth **412**, 54 (2015).

[15] M. Hu, J. He, Z. Zhao, T. A. Strobel, W. Hu, D. Yu, H. Sun, L. Liu, Z. Li, M. Ma *et al.*, Compressed glassy carbon: An ultrastrong and elastic interpenetrating graphene network, Sci. Adv. **3**, e1603213 (2017).

[16] S. Wong, T. B. Shiell, B. A. Cook, J. E. Bradby, D. R. McKenzie, and D. G. McCulloch, The shear-driven transformation mechanism from glassy carbon to hexagonal diamond, Carbon **142**, 475 (2019).

[17] Z. Li, Y. Wang, M. Ma, H. Ma, W. Hu, X. Zhang, Z. Zhuge, S. Zhang, K. Luo, Y. Gao *et al.*, Ultrastrong conductive *in situ* composite composed of nanodiamond incoherently embedded in disordered multilayer graphene, Nat. Mater. **22**, 42 (2023).

[18] C. de Tomas, I. Suarez-Martinez, and N. A. Marks, Graphitization of amorphous carbons: A comparative study of interatomic potentials, Carbon **109**, 681 (2016).

[19] T. B. Shiell, D. G. McCulloch, J. E. Bradby, B. Haberl, R. Boehler, and D. R. McKenzie, Nanocrystalline hexagonal diamond formed from glassy carbon, Sci. Rep. **6**, 37232 (2016).

[20] Z. Zeng, J. Wen, H. Lou, X. Zhang, L. Yang, L. Tan, B. Cheng, X. Zuo, W. Yang, W. L. Mao *et al.*, Preservation of high-pressure volatiles in nanostructured diamond capsules, Nature (London) **608**, 513 (2022).

[21] P. J. F. Harris, Fullerene-related structure of commercial glassy carbons, Philos. Mag. **84**, 3159 (2004).

[22] T. B. Shiell, S. Wong, W. Yang, C. A. Tanner, B. Haberl, R. G. Elliman, D. R. McKenzie, D. G. McCulloch, and J. E. Bradby, The composition, structure and properties of four different glassy carbons, J. Non-Cryst. Solids **522**, 119561 (2019).

[23] H. Hwang, Y. Bang, J. Choi, H. Cynn, Z. Jenei, W. J. Evans, A. Ehnes, I. Schwark, K. Glazyrin, G. D. Gatta *et al.*, Graphite resistive heated diamond anvil cell for simultaneous high-pressure and high-temperature diffraction experiments, Rev. Sci. Instrum. **94**, 083903 (2023).

[24] O. L. Anderson, D. G. Isaak, and S. Yamamoto, Anharmonicity and the equation of state for gold, J. Appl. Phys. **65**, 1534 (1989).

[25] X. Chen, H. Lou, Z. Zeng, B. Cheng, X. Zhang, Y. Liu, D. Xu, K. Yang, and Q. Zeng, Structural transitions of 4:1 methanol–ethanol mixture and silicone oil under high pressure, Matter Radiat. Extremes **6**, 038402 (2021).

[26] C. Prescher and V. B. Prakapenka, DIOPTAS: A program for reduction of two-dimensional x-ray diffraction data and data exploration, High Pressure Res. **35**, 223 (2015).

[27] J. Robertson, Diamond-like amorphous carbon, Mater. Sci. Eng., R **37**, 129 (2002).

[28] G. Kresse and J. Hafner, *Ab initio* molecular dynamics for liquid metals, Phys. Rev. B **47**, 558 (1993).

[29] P. E. Blöchl, Projector augmented-wave method, Phys. Rev. B **50**, 17953 (1994).

[30] J. Klimeš, D. R. Bowler, and A. Michaelides, Van der Waals density functionals applied to solids, Phys. Rev. B **83**, 195131 (2011).

[31] See Supplemental Material at http://link.aps.org/supplemental/10.1103/PhysRevB.109.214113 for potential energy as a function of temperature during the quenching process of liquid carbon in NVT *ab initio* MD simulation, calculated VDOS of GC and ta-C, and which includes Refs. [32,33].

[32] R. Cappelletti, T. Udovic, H. Li, and R. Paul, Glassy carbon, NIST Standard Reference Material (SRM 3600): Hydrogen content, neutron vibrational density of states and heat capacity, J. Appl. Crystallogr. **51**, 1323 (2018).

[33] G. C. Sosso, V. L. Deringer, S. R. Elliott, and G. Csányi, Understanding the thermal properties of amorphous solids using machine-learning-based interatomic potentials, Mol. Simul. **44**, 866 (2018).

[34] H. Muhli, X. Chen, A. P. Bartok, P. Hernández-León, G. Csányi, T. Ala-Nissila, and M. A. Caro, Machine learning force fields based on local parametrization of dispersion interactions: Application to the phase diagram of C_{60}, Phys. Rev. B **104**, 054106 (2021).

[35] M. A. Caro, V. L. Deringer, J. Koskinen, T. Laurila, and G. Csányi, Growth mechanism and origin of high sp^3 content in tetrahedral amorphous carbon, Phys. Rev. Lett. **120**, 166101 (2018).

[36] V. L. Deringer and G. Csányi, Machine learning based interatomic potential for amorphous carbon, Phys. Rev. B **95**, 094203 (2017).

[37] D. K. L. Tsang, B. J. Marsden, S. L. Fok, and G. Hall, Graphite thermal expansion relationship for different temperature ranges, Carbon **43**, 2902 (2005).

[38] W. L. Mao, H.-k. Mao, P. J. Eng, T. P. Trainor, M. Newville, C.-c. Kao, D. L. Heinz, J. Shu, Y. Meng, and R. J. Hemley, Bonding changes in compressed superhard graphite, Science **302**, 425 (2003).

[39] L. Wang, B. Liu, H. Li, W. Yang, Y. Ding, S. V. Sinogeikin, Y. Meng, Z. Liu, X. C. Zeng, and W. L. Mao, Long-range ordered carbon clusters: A crystalline material with amorphous building blocks, Science **337**, 825 (2012).

[40] X. Yang, M. Yao, X. Wu, S. Liu, S. Chen, K. Yang, R. Liu, T. Cui, B. Sundqvist, and B. Liu, Novel superhard sp^3 carbon allotrope from cold-compressed C_{70} peapods, Phys. Rev. Lett. **118**, 245701 (2017).

[41] A. C. Ferrari and J. Robertson, Interpretation of Raman spectra of disordered and amorphous carbon, Phys. Rev. B **61**, 14095 (2000).

[42] A. Ferrari and J. Robertson, Raman spectroscopy of amorphous, nanostructured, diamond-like carbon, and nanodiamond, Philos. Trans. R. Soc., Ser. A **362**, 2477 (2004).

[43] A. C. Ferrari and J. Robertson, Resonant Raman spectroscopy of disordered, amorphous, and diamondlike carbon, Phys. Rev. B **64**, 075414 (2001).

[44] J. Bruley, D. B. Williams, J. J. Cuomo, and D. P. Pappas, Quantitative near-edge structure analysis of diamond-like carbon in the electron microscope using a two-window method, J. Microsc. **180**, 22 (1995).

[45] P. K. Chu and L. Li, Characterization of amorphous and nanocrystalline carbon films, Mater. Chem. Phys. **96**, 253 (2006).

[46] V. V. Brazhkin and A. G. Lyapin, Hard and superhard carbon phases synthesized from fullerites under pressure, J. Superhard Mater. **34**, 400 (2012).

[47] D. G. McCulloch, S. Wong, T. B. Shiell, B. Haberl, B. A. Cook, X. Huang, R. Boehler, D. R. McKenzie, and J. E. Bradby, Investigation of room temperature formation of the ultra-hard nanocarbons diamond and lonsdaleite, Small **16**, 2004695 (2020).

[48] J. Dong, Z. Yao, M. Yao, R. Li, K. Hu, L. Zhu, Y. Wang, H. Sun, B. Sundqvist, K. Yang *et al.*, Decompression-induced diamond formation from graphite sheared under pressure, Phys. Rev. Lett. **124**, 065701 (2020).

[49] X. Huang, T. B. Shiell, A. Salek, A. Aghajamali, I. Suarez-Martinez, Q. Sun, T. A. Strobel, D. R. McKenzie, N. A. Marks, D. G. McCulloch *et al.*, Comparison of hydrostatic and non-hydrostatic compression of glassy carbon to 80 GPa, Carbon **219**, 118763 (2024).